BRAIN
A JOURNAL OF NEUROLOGY

Mutations in *C1orf194*, encoding a calcium regulator, cause dominant Charcot-Marie-Tooth disease

Shun-Chang Sun,[1],* Di Ma,[2],* Mei-Yi Li,[2],* Ru-Xu Zhang,[3],* Cheng Huang,[2]
Hua-Jie Huang,[2] Yong-zhi Xie,[3] Zhong-Ju Wang,[2] Jun Liu,[4] De-Cheng Cai,[2] Cui-Xian Liu,[2]
Qi Yang,[2] Fei-Xiang Bao,[5] Xiao-Li Gong,[2] Jie-Ru Li,[2] Zheng Hui,[6] Xiao-feng Wei,[2]
Jian-Mei Zhong,[2] Wan-jun Zhou,[2] Xuan Shang,[2] Cheng Zhang,[7] Xing-Guo Liu,[5]
Bei-Sha Tang,[3] Fu Xiong[2,8,9] and Xiang-Min Xu[2,8,9,10]

*These authors contributed equally to this work.

Charcot-Marie-Tooth disease is a hereditary motor and sensory neuropathy exhibiting great clinical and genetic heterogeneity. Here, the identification of two heterozygous missense mutations in the *C1orf194* gene at 1p21.2-p13.2 with Charcot-Marie-Tooth disease are reported. Specifically, the p.I122N mutation was the cause of an intermediate form of Charcot-Marie-Tooth disease, and the p.K28I missense mutation predominately led to the demyelinating form. Functional studies demonstrated that the p.K28I variant significantly reduced expression of the protein, but the p.I122N variant increased. In addition, the p.I122N mutant protein exhibited the aggregation in neuroblastoma cell lines and the patient's peroneal nerve. Either gain-of-function or partial loss-of-function mutations to C1ORF194 can specify different causal mechanisms responsible for Charcot-Marie-Tooth disease with a wide range of clinical severity. Moreover, a knock-in mouse model confirmed that the *C1orf194* missense mutation p.I121N led to impairments in motor and neuromuscular functions, and aberrant myelination and axonal phenotypes. The loss of normal C1ORF194 protein altered intracellular Ca^{2+} homeostasis and upregulated Ca^{2+} handling regulatory proteins. These findings describe a novel protein with vital functions in peripheral nervous systems and broaden the causes of Charcot-Marie-Tooth disease, which open new avenues for the diagnosis and treatment of related neuropathies.

1 Department of Clinical Laboratory, Ruijin Hospital North, Shanghai Jiao Tong University School of Medicine, Shanghai, P.R. China
2 Department of Medical Genetics, School of Basic Medical Sciences, Southern Medical University, Guangzhou, P.R. China
3 Department of Neurology, Xiangya Hospital, Central South University, Changsha, Hunan 410008, P.R. China
4 Department of Neurology and Institute of Neurology, Ruijin Hospital, Shanghai Jiao Tong University School of Medicine, Shanghai, P.R. China
5 Key Laboratory of Regenerative Biology, Guangdong Provincial Key Laboratory of Stem Cell and Regenerative Medicine, South China Institute for Stem Cell Biology and Regenerative Medicine, Guangzhou Institutes of Biomedicine and Health, Chinese Academy of Sciences, Guangzhou, P.R. China
6 Department of Neurology, Nanfang Hospital, Southern Medical University, Guangzhou, P.R. China
7 Department of Neurology, First Affiliated Hospital, Sun Yat-sen University, Guangzhou, P.R. China
8 Guangdong-Hong Kong-Macao Greater Bay Area Center for Brain Science and Brain-Inspired Intelligence, Guangzhou 510515, P.R. China
9 Guangdong Provincial Key Laboratory of Single Cell Technology and Application, Guangzhou, Guangdong Province, P.R.China
10 Key Laboratory of Mental Health of the Ministry of Education, Guangdong-Hong Kong-Macao Greater Bay Area Center for Brian Science and Brain-Inspired Intelligence, Southern Medical University, Guangzhou 510515, P.R. China

Correspondence to: Fu Xiong
Department of Medical Genetics, School of Basic Medical Sciences, Southern Medical University,
Guangzhou, P.R. China
E-mail: xiongfu@smu.edu.cn

Correspondence may also be addressed to: Xiang-Min Xu
E-mail: gzxuxm@pub.guangzhou.gd

Introduction

Charcot-Marie-Tooth (CMT) disease, which is also known as hereditary motor and sensory neuropathy, is the most common type of inherited peripheral neuropathy, with an estimated prevalence of 10–40 cases/100 000 population (Hoyle *et al.*, 2015; Barreto *et al.*, 2016) (http://neuromuscular.wustl.edu/time/hmsn.html). CMT disease exhibits considerable clinical and genetic heterogeneity, and is characterized by progressive length-dependent peripheral neuropathy resulting in distal muscle weakness and atrophy, foot deformities, distal sensory loss, and the absence of reflexes (Hoyle *et al.*, 2015; Pareyson *et al.*, 2017). CMT is divided into the demyelinating type (CMT1), the axonal defective type (CMT2), and an intermediate type (DI-CMT), which is characterized by demyelination and axonal loss. Up to now, more than 90 genes have been associated with CMT and related neuropathies, which has led to a better understanding of neuronal physiology and the establishment of the foundations for a novel molecular classification system, diagnostic testing methods, and promising therapeutic targets. In particular, *PMP22*, *GJB1*, *MPZ*, *MFN2*, and *GDAP1* are the most common genes responsible for genetically confirmed CMT (Hoyle *et al.*, 2015; Pareyson *et al.*, 2017; Lassuthova *et al.*, 2018). However, the underlying genetic cause of CMT remains unknown in 47–75% of affected families (Rossor *et al.*, 2013).

A series of remarkable studies have proposed frameworks for various pathogenic mechanisms of different types of CMT disease involving peripheral neurons and Schwann cells, including abnormities in myelin assembly, cytoskeleton stabilization, membrane trafficking, mitochondrial dynamics, axonal transport, and RNA metabolism (Harel and Lupski, 2014; Prior *et al.*, 2017). In particular, the disruption of Ca^{2+} homeostasis has been identified as an important causative factor in the pathophysiology of CMT disease (Villegas *et al.*, 2014; Gonzalez-Sanchez *et al.*, 2017). It has verified that an excessive influx of cytoplasmic Ca^{2+} is associated with demyelination and axonal degeneration (Zhang and David, 2016). Mutations in *TRPV4* mediating Ca^{2+} influx, lead to intracellular toxic effects (Donate-Macian *et al.*, 2018). PMP22-mediated overexpression of the P2X7 purinoceptor, resulting in high intracellular Ca^{2+} concentrations in Schwann cells, is a cause of CMT1A (Sociali *et al.*, 2016).

In the present study, the heterozygous missense mutation c.365T > A (p.I122N) in the *C1orf194* gene responsible for dominant intermediate CMT (DI-CMT) disease in a large family was identified and further confirmed by linkage analysis. Subsequently, the heterozygous missense mutation c.83A > T (p.K28I) to *C1orf194* was identified in 1/107 Chinese individuals with CMT disease. Functional studies of these two CMT-causing mutations were performed using a p.I121N knock-in mouse model with recapitulated neuropathy similar to that exhibited by index patients with CMT disease. Moreover, we further showed that *C1orf194* mutation disrupted neuromuscular functions, likely through the dysregulation of Ca^{2+} homeostasis, which leads to axon demyelination and subsequent degeneration.

Materials and methods

Subjects, clinical assessment, and whole exome sequencing

The study protocol was approved by the Medical Ethics Committee of Southern Medical University (Guangzhou, China) and conducted in accordance with the Declaration of Helsinki. Written informed consent was obtained from all participants or their guardians before enrolment in this study. The members of two studied families underwent complete neurological examinations by neurologists based on the clinical guidelines of the European CMT consortium. The probands underwent electrophysiological examinations and other family members were assessed retrospectively. Whole exome sequencing of DNA from five individuals (two normal individuals: Subjects III-6 and III-9; three affected individuals: Patients IV-1, IV-5 and IV-8) from Family 1 and the proband (Patient III-2) from Family 2 (Fig. 1A) was performed to identify variants as previously described (Yang *et al.*, 2016). Sanger sequencing was performed to determine whether the potentially causative mutations identified by whole exome sequencing were co-segregated with the CMT phenotype in Family 1.

C1orf194 mutation screening

To determine whether *C1orf194* mutations were present in other patients with CMT disease, 107 DNA samples from 37 familial and 70 sporadic cases of CMT disease that were
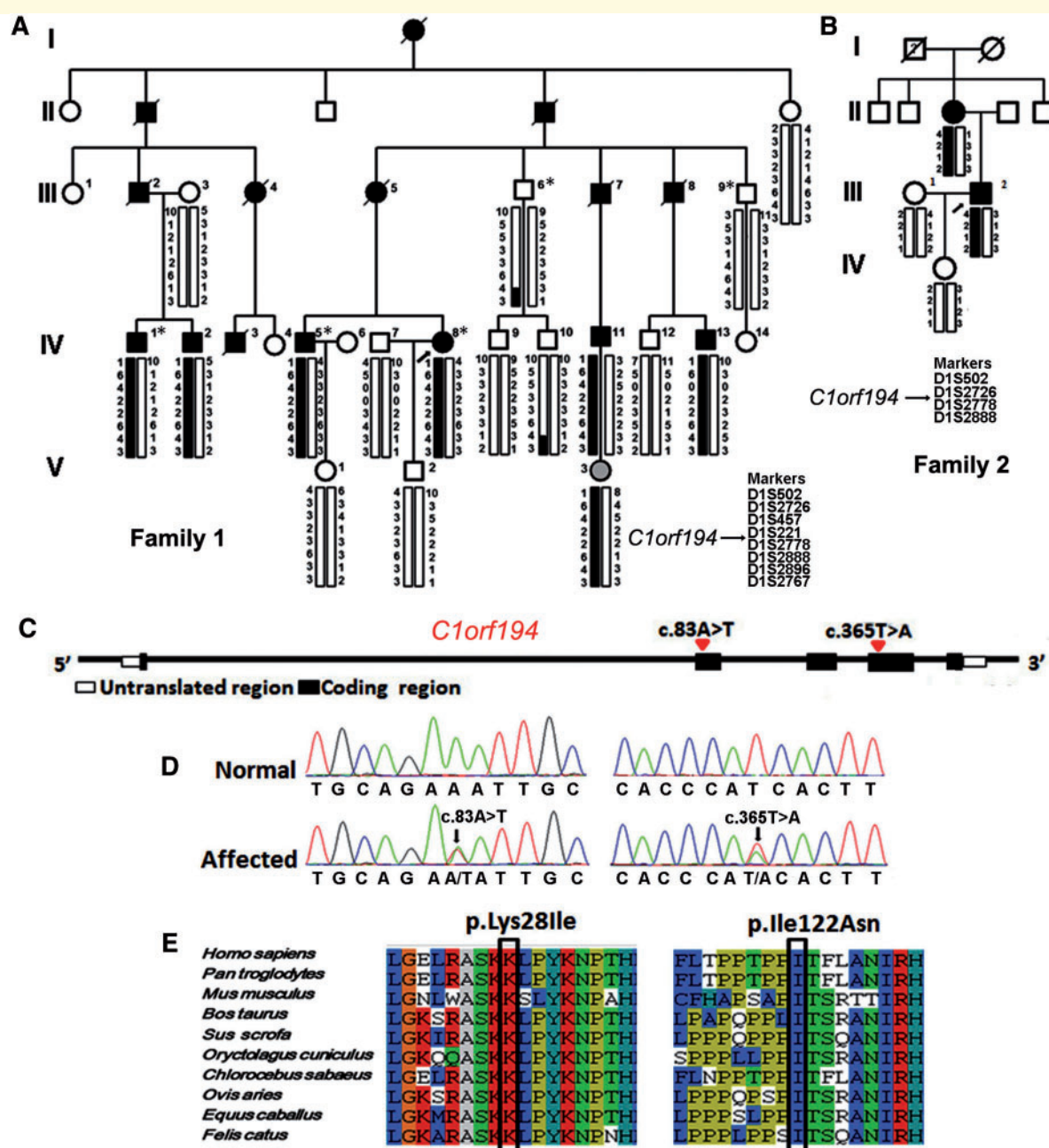
Figure 1 Pedigree-based mapping and identification of CMT-causing mutations in *C1orf194*. (**A**) Pedigree-based linkage study of 17 individuals selected from 32 subjects in Family 1 (F1). The segregating haplotype associated with CMT is indicated by a box with eight polymorphic microsatellite markers on 1p21.2-p13.2. The five family members consisting of three affected subkects and two healthy controls recruited for whole exome sequencing are marked by asterisks. (**B**) An additional family (Family 2; F2) was recruited for confirmatory mapping of the given genome region associated with CMT and mutation detection. Arrow = proband; filled square = affected individuals; black vertical bar = disease-associated haplotypes. *C1orf194* is flanked by D1S221 and D1S2778 in Family 1 or by D1S2726 and D1S2778 in Family 2. (**C**) A physical map of the region encompassing *C1orf194* and the positions of identified two mutations in *C1orf194* are indicated by red inverted triangles. (**D**) Chromatograms of the genomic sequence of the two mutations. The *top* and *bottom* diagrams show normal and mutated sequences, respectively, and the arrow indicates the heterozygous state. (**E**) Amino acid sequence alignment of the *C1orf194* orthologues. The lysine (K) residue at position 28 and the isoleucine (I) residue at position 122 are highly conserved from humans to *Felis catus*.

collected in Southern China were analysed. Genomic DNA was extracted from peripheral blood using standard techniques. Primers were designed to amplify the coding exons and intron-exon boundaries of *C1orf194*. Short tandem

repeat markers (D1S502, D1S2726, D1S457, D1S221, D1S2778, D1S2888, D1S2896, and D1S2767), which flank *C1orf194*, were selected for co-segregation analysis. Candidate mutations that co-segregated with CMT patients

were further assessed by high-resolution melting analysis in 500 unrelated normal controls with matched geographical ancestry.

Plasmid constructs

Full length *C1orf194* cDNA was amplified from human spinal cord tissues by reverse transcription PCR (RT-PCR) and subsequently cloned into pcDNA3.1-FLAG or pTurboFP635-C expression vectors by double digestion with HindIII and EcoI (New England Biolabs). The c.365T>A and c.83A>T mutations were then introduced into wild-type *C1orf194* plasmids by PCR-based site-directed mutagenesis. Recombinant plasmids were purified with the Endo-Free Plasmid Midi Kit (Omega Bio-Tek) and confirmed by Sanger sequencing.

Subcellular location

Cells lines were cultured in Dulbecco's modified Eagle medium (Gibco) supplemented with 10% foetal bovine serum. Recombinant wild-type and mutant pTurboFP635-C plasmid constructions of *C1orf194* were transfected into human neuroblastoma (SK-N-SH) and mouse neuroblastoma (Neuro2a) cell lines with the 4D-Nucleofecor$^{\text{TM}}$ System (Lonza) or Lipofectamine$^{\text{TM}}$ 2000 reagent (Invitrogen), respectively. At 24 h post transfection, cell nuclei were then counterstained with 4′,6-diamidino-2-phenylindole (DAPI; Sigma-Aldrich) to observe the subcellular location of the C1ORF194 protein. After staining, the cells were viewed under a confocal fluorescence microscope (LSM 880; Carl Zeiss AG). Transfected Neuro2a cells were double stained with α-tubulin antibody (Abcam) followed by fluorescein isothiocyanate (FITC)-conjugated secondary antibodies (Sigma-Aldrich).

Detection of human *C1orf194* expression

Total RNA was extracted with TRIzol® reagent (Invitrogen) from white blood cells collected from normal individuals and the affected individuals (Family 1, IV-5 and IV-8; Family 2, III-2). *C1orf194* mRNA expression levels were analysed using the GoTaq® qPCR Master Mix System (Promega) with the specific primer pair (F) 5′-CTTAGGAGAACTGCGGGCTT-3′ and (R) 5′-GTCATCCTTTGGTATCTCGGG-3′. Gene expression levels were calculated using the $2^{-\Delta\Delta CT}$ method. Expression levels of the target genes were normalized to that of *GAPDH* with the specific primer pair (F) 5′-GTGAAGGTCGGAGTCAACG-3′ and (R) 5′-TGAGGTCAATGAAGGGGTC-3′. The mRNA levels were quantified with the CFX96 Touch$^{\text{TM}}$ QPCR System (Bio-Rad). Moreover, qRT-PCR was performed to determine the expression patterns of human *C1orf194* mRNA in the spinal cord, sciatic nerve, lung, gastrocnemius muscle, cerebrum, cerebellum, liver, kidney, and heart.

Western blot analysis

To determine whether C1ORF194 protein expression was influenced by the variants, 293T cells were transfected with the plasmids pcDNA3.1-FLAG, pcDNA3.1-FLAG-C1ORF194, pcDNA3.1-FLAG-I122N, and pcDNA3.1-FLAG-K28I with Lipofectamine$^{\text{TM}}$ 2000 (Invitrogen). For C1ORF194 degradation study, at 24 h post transfection, 100 µg/ml of cycloheximide (Sigma-Aldrich) were added to each well and then total cell protein was collected at 0, 1, 3, 5, and 7 h to evaluate the half-life of the C1ORF194 protein. Cell cultures as well as human and mouse tissues were lysed with radioimmunoprecipitation assay buffer (Cell Signaling Technology) supplemented with protease inhibitor cocktail (Sigma-Aldrich). The lysates were centrifuged, quantified by the bicinchoninic acid (BCA) assay (Thermo Fisher Scientific), and boiled with protein loading buffer before separation by sodium dodecyl sulphate polyacrylamide gel electrophoresis (SDS-PAGE) and transferred to polyvinylidene fluoride membranes (EMD Millipore). Then, the membranes were blocked with 5% non-fat milk for 1 h and incubated overnight at 4°C with mouse monoclonal FLAG antibody (F1804; dilution, 1:1000; Sigma-Aldrich), mouse monoclonal β-actin antibody, mouse monoclonal GAPDH antibody, and rabbit polyclonal C1ORF194 antibody (ab121937, Abcam; 1:500 dilution). The next day, the membranes were incubated with horseradish peroxidase-conjugated secondary antibodies (Abcam) for 2 h. Proteins were detected using an electrochemiluminescence kit (Thermo Fisher Scientific) and imaged with a digital chemiluminescence system (Tanon Science & Technology Co., Ltd.). Western blot analysis was repeated three times for each test and the expression levels of the targeted protein were normalized to that of β-actin or GAPDH.

Ca^{2+} assay

The Ca^{2+} sensitive fluorescent dye Fluo-3/AM and Rhod-2 (Yeasen) was used to detect cytoplasm and mitochondria Ca^{2+} levels, respectively. Briefly, stable SH-SY5Y cell lines grown on confocal dish were washed twice with D-Hank's buffered salt solution and incubated with 4 µM Fluo-3/AM or 2 µM Rhod-2 AM at 37°C for 30 min in the dark. Afterwards, the cells were washed three times with D-Hank's buffered salt solution and further incubated with D-Hank's buffer at 37°C for 30 min. Finally, signals were collected with a confocal laser scanning microscope (LSM 880 with Airyscan) using a ×20 water immersion lens at 488 nm (Fluo-3, AM) and 590 nm (Rhod-2), respectively. Cytoplasmic and mitochondrial Ca^{2+} concentrations were recorded by mean fluorescence intensity (Fbase). The fluorescence intensity variation was recorded from an average of 10–20 cells per experiment. For cytoplasmic Ca^{2+} measurement, IMR-32 cells (human neuroblastoma) was transfected with recombinant K28I plasmid were trypsinized, collected, and washed twice with D-Hank's buffered salt solution. Then, the cells were incubated with 2 µM Fluo-3/AM at 37°C for 30 min in the dark and washed three times with D-Hank's buffered salt solution. Finally, cytosolic Ca^{2+} was analysed by flow cytometry.

Intracellular ATP content assay

SH-SY5Y cell lines with wild-type or mutant C1ORF194 were harvested, resuspended, and counted. The amount of ATP was measured by incubating cells with 100 µl of luciferin/luciferase using the CellTiter-Glo® Luminescent Cell Viability Assay (Promega). Sample luminescence was quantified and expressed as fold over control. Each condition was evaluated in duplicate and experiments were repeated at least three times.

Generation of p.I121N knock-in mice

C1orf194 homologue knock-in mice were constructed by the Nanjing Biomedical Research Institute with a CRISPR/Cas9 system (Supplementary Fig. 4A) as reported previously (Delphine *et al.*, 2018). Briefly, the c.362 T > A mutation in the NM_029314 transcript of *1700013F07Rik* (the mouse homologue of human *C1orf194*) was introduced into a bacterial artificial chromosome clone. Embryonic stem cells were obtained from C57BL/6 J mice. Chimeric mice (F0) were selected and confirmed by PCR and DNA sequencing (Supplementary Fig. 4B). The *C1orf194*^{+/+}, *C1orf194*[+/I121N], and *C1orf194*[I121N/I121N] mice used throughout this study were from a F1 *C1orf194*[+/I121N] self-crossed inbred line. Mice were maintained in a specific pathogen-free animal facility under a 12-h light/dark cycle. All protocols involving the use of animals were conducted in accordance with the approved guidelines of the Institutional Animal Care and Use Committee of Southern Medical University.

Genotyping and *C1orf194* expression analysis

Mouse genomic DNA was isolated from tail biopsy samples and extracted with a mouse tail DNA purification kit (Promega). PCR was performed with the primer pair (F) 5′-TGTACCACGGAGCTACATCC-3′ and (R) 5′-GAAAAGAGAACGGGGTGAGC-3′ with Kod FX polymerase (Toyobo). Sanger sequencing was performed to identify the three different genotypes of the mice. The cDNA from mice on embryonic Days 7, 15, and 17 were from Clontech Laboratories. In addition, whole-brain tissue from wild-type mice at postnatal Days 1, 2, 3, 4, 7, 8, 9, 10, 13, 15, and 16, as well as adult mice was quickly dissected on ice. The mRNA was extracted as mentioned above and qRT-PCR was performed to determine *C1orf194* mRNA expression patterns in the spinal cord, sciatic nerve, lung, gastrocnemius muscle, cerebrum, cerebellum, liver, kidney, spleen, and heart. Moreover, wild-type and mutant mice were sacrificed and the cerebrum, cerebellum, sciatic nerves, and gastrocnemius muscles were collected and used for immunoblotting to analyse the relative abundance of the C1ORF194 protein.

Behavioural experiments

Weight

A minimum of 20 wild-type and transgenic male mice, aged 3, 4, 5, and 7 months, were weighed.

Hind limb extension test

All mice underwent the hind limb extension test at the ages of 4 months as reported previously (Yang *et al.*, 2016). Briefly, the mice were suspended by the tail and hind limb extension was observed for 10 s. A score of 2 corresponded to a normal extension reflex of the hind limbs with splaying of the toes. A score of 1 corresponded to clenching of the hind limbs to the body with partial splaying of the toes. A score of 0 corresponded to clasping the hind limbs with the toes curled. A score of 1.5 or 0.5 corresponded to behaviours between 2 and 1 or 1 and 0, respectively. The test was performed three times at 30-s intervals for each mouse.

Gait analysis

Gait parameters were measured using a clear perspex apparatus (65 × 5 × 15 cm) with white paper covering the floor and a darkened box at the end. The hind paws were painted with non-toxic black ink. At least three consecutive footprints were used to assess gait abnormalities on both sides, which included stride length, stride width, stride angle, and the degree of toe spreading. The parameters were averaged for statistical analysis. Disease progression in the mice was assessed at 4 months.

Grip strength

Mice aged 4 and 8 months were placed on the centre of a power meter and the tails of the mice were pulled to force them off the power meter. The readings of the power meter were recorded and each mouse was tested seven times. The average value of the holding power was used as a representative value for statistical analysis.

Rotarod test

Motor coordination was measured via the latency to fall from a rotarod apparatus. Animals aged 4 and 8 months underwent 3 days of training on a rotarod apparatus at a constant speed of 15 rpm. Each of the training sessions lasted no more than 5 min. The mice were then tested on the apparatus at a constant speed of 25 rpm for three trials with a 30-min break between each trial. The latency to fall from the rotarod was recorded for each trial and the averaged times were used for statistical analysis.

Morphological study

Electron microscopy

The distal sciatic nerves of five mice aged 4 months of each genotype were dissected, fixed in 2.5% glutaraldehyde, and post-fixed in 1% OsO_4. After dehydration in a series of graded acetone, the samples were embedded in epoxy resin and then cut into ultrathin sections (70 nm), which were counterstained with 2% uranyl acetate and lead citrate. The stained ultrathin sections were observed with a transmission electron microscope (JEM-2010). ImageJ software (https://imagej.nih.gov/ij/) was used to assess the following parameters: (i) myelin thickness; (ii) axonal diameter; (iii) G-ratio of the myelinated nerve fibre (axon diameter divided by the total fibre diameter); and (iv) abnormal myelin ratio. In addition, the shapes of peripheral nerve axons and myelin sheath, and the numbers and arrangements of the myelin layers and other organelle structures were also observed.

Immunofluorescence assay of teased fibres

Teased fibres of the sciatic nerve were prepared before immunofluorescence analysis. Sciatic nerves were dissected from wild-type and knock-in mice at the age of 4 months and fixed in 4% paraformaldehyde for 6 h. After fixation, the paraformaldehyde was removed and the nerves were immersed in fresh cold phosphate-buffered saline at 4°C overnight and teasing was begun the following day. After the teased fibres were air dried, the sections were permeabilized with cold (−20°C) methanol for 15 min, incubated with blocking buffer (5% bovine serum albumin, 0.5% Triton™ X-100) at room temperature for 1 h, followed by incubation with primary

antibodies (NFH200; #N4142; Sigma-Aldrich) diluted in blocking buffer overnight at 4°C and then for 2 h with FITC-conjugated secondary antibodies at room temperature. Finally, the teased fibre sections were mounted with anti-fade fluorescence mounting medium with DAPI. The internodal length and Schmidt-Lanterman incisures were measured with ImageJ software.

Haematoxylin and eosin, Oil red O, and Masson trichrome staining

Gastrocnemius muscle and sciatic nerves were dissected. The gastrocnemius muscle sections were stained with HE and cut into cryosections before Oil red O staining and counterstaining with HE. The sciatic nerves were serially sectioned and then routinely stained with Masson's trichrome for histopathological examination.

Proteomics study

The sciatic nerve samples of eight $C1orf194^{+/+}$, $C1orf194^{+/I121N}$ mice at the age of 6 months were pooled into two groups, respectively. Proteins were homogenized with lysis buffer (7 M urea, 2 M thiourea, 0.2% SDS, 20 mM Tris base) containing protease inhibitor compound and then precipitated with acetone. SDS-PAGE was performed to assess the protein quality after quantification with the BCA assay. Proteins differentially expressed between the wild-type and CMT mice were analysed by isobaric tag for relative and absolute quantification (iTRAQ) proteomics technology. Total protein (100 μg) was incubated with Trypsin Gold (Promega) at a protein: trypsin ratio of 50:1 at 37°C overnight and then supplemented with trypsin (1:100) the next morning and incubated for an additional 4 h. The iTRAQ reagent from the 8-plex iTRAQ kit (AB SCIEX) was used to label the samples according to the manufacturer's protocol. Next, liquid chromatography-tandem mass spectrometry (LC-MS/MS) was performed and data were searched against the International Protein Index mouse sequence database included with the Protein Pilot™ software 5.0 package. User-defined parameters and false discovery rates for assignment of the peptides and proteins were set. Unused ProtScore ⩾1.3 was used as the qualification criterion (corresponding to a confidence limit of 95%). Only proteins with fold changes >1.5 were considered to be differentially expressed. In the repeated experiment for each sample, the test methods and markings were exactly the same. The differentially expressed proteins were analysed further for functional annotation with online DAVID software (http://david.abcc.ncifcrf.gov).

Statistical analyses

Statistical analyses were performed with GraphPad software. Statistical differences among the three groups were determined using one-way analysis of variance followed by Bernoulli correction. Statistical differences between any two groups were determined using the independent t-test. Data are presented as the mean ± standard error of the mean. For all analyses, statistical significance is denoted as *P < 0.05, **P < 0.01, or ***P < 0.001.

Data availability

The authors confirm that the data supporting the findings of this study are available within the article and its Supplementary material.

Accession codes

Human $C1orf194$ (BC150515.1), GRCh38/hg38 chr1: 109108 036T>A (c.83A>T (p.K28I)), GRCh38/hg38 chr1:10910660 9A>T (c.365T>A (p.I122N), mouse $C1orf194$ (NM_0293 14). ClinVar accessions: ss2137543879, ss2137543880.

Results

Mapping and identification of $C1orf194$ mutations

Seventeen members from a large Chinese family (Fig. 1A, Family 1) in a five-generation pedigree with autosomal dominant intermediate CMT (DI-CMT) were selected for pedigree-based gene mapping. Linkage analysis of microsatellite repeats in Family 1 showed significant linkages to chromosome 1p21.2-p13.2 and a maximum logarithm of the odds (LOD) score of 4.11 (Fig. 1A), which was also validated in another family (Fig. 1B). Meanwhile, to identify the underlying genetic defects, whole exome sequencing of five family members from Family 1, including three affected individuals, was performed. Sanger sequencing (Fig. 1D), found that the $C1orf194$ missense mutation c.365T>A (p.I122N) co-segregated with the CMT phenotype in the family members (Supplementary Fig. 1). In addition, we ruled out the previously reported candidate region for CMT by haplotype linkage analysis (data not shown) and obtained negative results for all known mutations in CMT-related genes including duplication/deletion of $PMP22$ based on the whole exome data. Moreover, the c.83A>T (p.K28I) mutation (Fig. 1D) was identified in two patients with familial CMT disease (Fig. 1B). Whole exome sequencing was also conducted for the proband of Family 2 (Fig. 1B, Patient III-2) and all were negative for known CMT-related genes. Figure 1C shows the $C1orf194$ gene and the locations of two different mutations examined. The c.83A>T and c.365T>A mutations were unreported in the National Center for Biotechnology Information database (https://www.ncbi.nlm.nih.gov/). Neither of these two mutations was detected in 500 ethnically matched unaffected individuals. The Lys28 and Ile122 residues of $C1orf194$ are highly conserved across species from Homo sapiens to Felis catus (Fig. 1E).

Patient phenotypes

A summary of the clinical and genetic characteristics of all eight patients (six from Family 1 and two from Family 2) are presented in Table 1 (Hoyle et al., 2015; Zhao et al., 2016; Berciano et al., 2017). The affected individuals had some clinical and phenotypic features of peripheral

Table 1 Clinical features of patients with *C1ORF194* mutations

Clinical records	Family1 (c.365T>A)						Family2 (c.83A>T)	
	IV-1	IV-2	IV-5	IV-8	IV-11	IV-13	III-2	II-2
Gender	Male	Male	Male	Female	Male	Male	Male	Female
Age of onset	20	31	28	31	33	31	6	40
Age at exam	24	33	36	34	35	31	34	56
Initial symptom	Impossible to run	Distal leg weakness	Distal leg weakness	Distal leg weakness	Impossible to walk quickly	Impossible to walk quickly	Gait insatiability	Gait insatiability
Distal muscle strength (UL/LL)	+ +/+ + +	+/+ +	+ +/+ + +	+ +/+ + +	-/+	-/+	+ +/+ +	+ +/+ +
Distal muscle atrophy (UL/LL)	+/+ +	+/+ +	+/+ +	+/+ +	-/+	-/+	+ + +/+ + +	+ +/+ +
Sensory disturbance (UL/LL)	Distal LL	LL	LL	LL	Distal LL	Distal LL	Distal UL	Distal UL
Tendon reflex	Absent	Absent	Absent	Absent	Hypoactive	Hypoactive	Absent	Absent
Pes cavus	No	No	No	No	No	No	Yes	Yes
Gait	Steppage	Steppage	Steppage	Steppage	No	No	Steppage	Steppage
MNCV, m/s/CAMP, mV								
Median	43.2/5.8	36.2/1.9	38.9/5.0	43.2/8.1	45.7/7.7	50.0/8.1	10.9/0.5	NA
Ulnaris	42.2/5.0	44.0/5.8	47.9/4.3	49.0/4.5	44.2/5.9	52.8/9.9	11.2/0.2	NA
Peroneus	30.0/4.8	37.0/2.0	37.5/6.0	41.9/2.3	37.6/9.5	38.8/10.0	NA	NA
SNCV, m/s/SNAP, μV								
Median	46.4/5.0	46.8/3.0	52.2/7.5	53.8/12.0	51.7/14.0	57.7/12.0	NA	NA
Ulnaris	47.8/8.9	43.3/3.0	50.0/7.9	54.5/8.7	50.0/12	56.5/7.5	NA	NA
CMTNS	17	15	16	15	3	3	>21	NA
NCS	DI-CMT	DI-CMT	DI-CMT	DI-CMT	DI-CMT	DI-CMT	CMT1	CMT unclassified[a]

Muscle strength: + = distal weakness 4/5 on Medical Research Council (MRC); + + = distal weakness <4/5 on MRC scale; + + + = S proximal weakness.
Muscle atrophy: + = mild atrophy in distal limbs; + + = moderate atrophy in distal limbs; + + + = severe distal limbs or proximal muscle atrophy.
[a]Cannot be classified because of incomplete clinical data.
CMAP = compound muscle action potential; CMTNS = CMT neuropathy score; CMT1/CMT2/DI-CMT = Charcot-Marie-Tooth disease type 1, type 2 and dominant intermediate type; LL = lower limbs; MNCV = motor nerve conduction velocity; NA = not available; NCS = nerve conduction study; SNAP = sensory nerve action potential; SNCV = sensory nerve conduction velocities; UL = upper limbs.

neuropathies, including symmetric atrophy and progressive weakness of the distal muscles (Fig. 2A and B), sensory loss or absent tendon reflexes, as well as pathological and electrophysiological abnormalities. The proband (Patient IV-8) of Family 1 was a 44-year-old female who walked with a bilateral steppage gait and had difficulties with climbing stairs. Moreover, the bilateral flexor and extensor muscles of the feet and toes were weak, as were the finger flexors, extensors, and abductor muscles. Deep tendon reflexes were absent in the lower extremities. Sensory examination showed diminished tactile and pain sensation in a stocking and glove pattern, and vibratory sensation was reduced distally in the lower limbs. Electrophysiological studies at 34 years of age revealed a length-dependent neuropathy with motor conduction velocities between 41.9 and 49.0 m/s. Her 46-year-old brother and four cousins had very similar complaints with an age of onset between 20 and 33 years. In addition, one individual carrying the *C1orf194* mutation (Patient V-3 in Family 1, a 2-year-old female) did not exhibit clinical phenotypes, presumably because of her very young age. The proband of Family 2 (Patient III-2) was a 34-year-old male. At the age of 6 years, he first presented with walking instability and had a tendency to fall. Subsequently, he developed weakness of the distal lower and upper limbs. At the age of 30 years, he developed difficulty running, going up stairs, getting up after squatting, and completing fine motor tasks. Vibratory sensation of the toes was reduced, pinprick sensation was absent in the feet, and decreased below the knees. Reflexes were symmetrically absent at the knees and ankles. He had a steppage gait and his exam was notable for high arched feet. His mother is a 56-year-old female and at the age of 40 years, she first noticed her disability with physical exercise due to distal foot muscle weakness. Subsequently, she developed distal upper limbs weakness with progressive gait disturbances, and difficulty with walking at the age of 50 years. She had obvious atrophy of the distal forearm, calf, peroneal, and foot muscles. Deep tendon reflexes were absent in the lower extremities. Sensory examination showed decreased superficial sensitivity in the regions distal to knees. Bilateral pes cavus, claw hand, and steppage gait were also noted. Based on motor nerve conduction velocity (MNCV), CMT disease is categorized as demyelinating (CMT1; MNCV <38 m/s), intermediate (MNCV = 25–45 m/s), and axonal (CMT2; MNCV >38 m/s). Therefore, the affected members of Families 1 and 2 were diagnosed with intermediate CMT disease and CMT1, respectively. Some of the typical
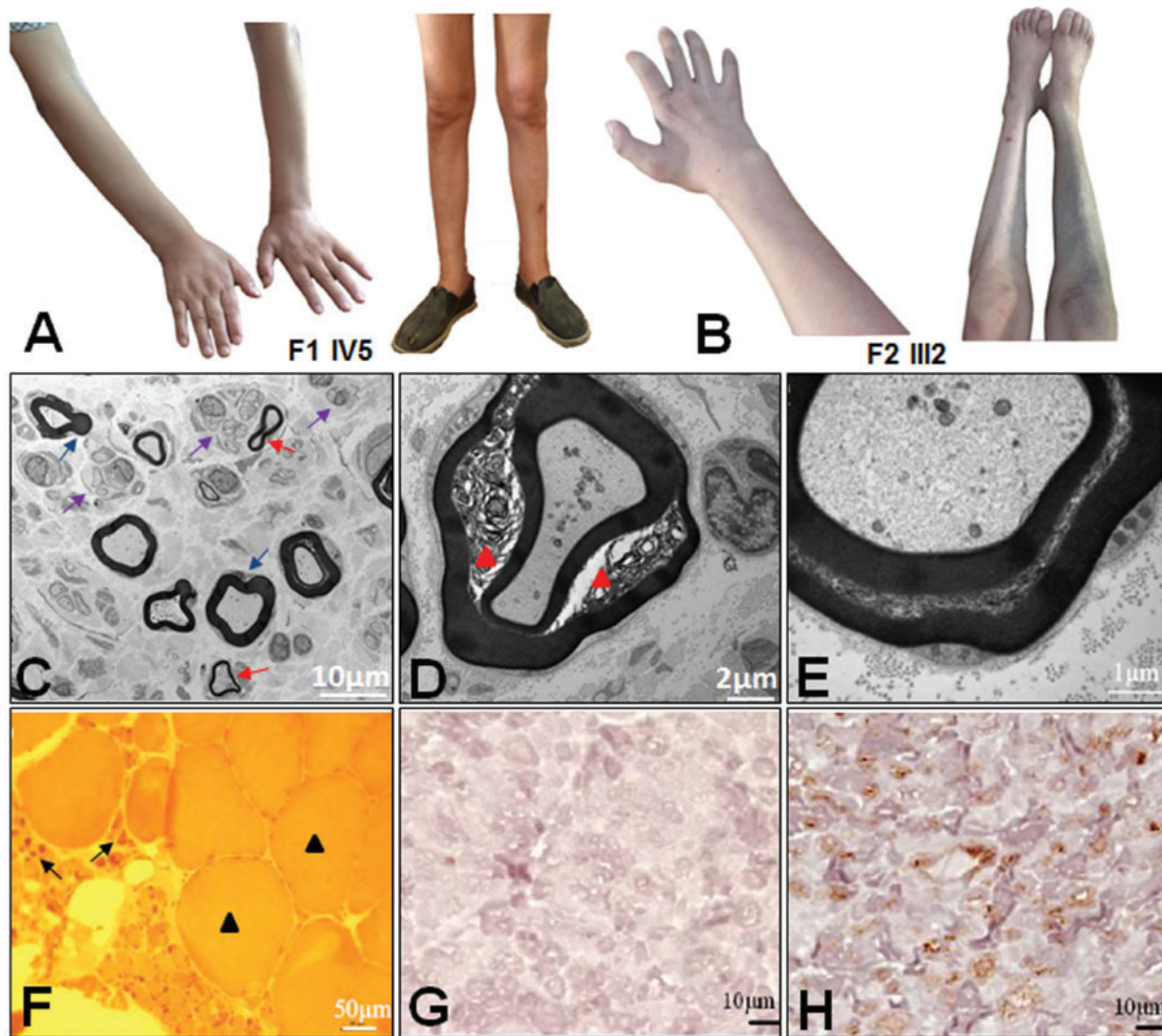
Figure 2 Several specific phenotypic characteristics associated with CMT. (**A** and **B**) Photographs of Patients F1-IV5 and F2-III2 showing severe muscle wasting in the legs and moderate muscle wasting in the hands. Patient F2-III2 had claw hands, pes excavatus, and crane legs. (**C**–**E**) Electron micrographs of cross sections of the peroneal nerves from Patient F1-IV5 exhibiting the typical pathological features of demyelination (red arrowheads), reduction of the myelin sheath thickness and irregular myelin sheath (red arrows), external myelin folding (blue arrows), and regeneration clusters (purple arrows). (**F**) A haematoxylin and eosin-stained biopsy section of the left tibialis anterior muscle of Patient F1-IV5 showing muscle atrophy (arrows) with hypertrophic (black arrowheads) and angulated fibres. (**G** and **H**) Immunohistochemically stained sections with anti-C1ORF194 antibody showed more C1ORF194 protein expression in the peroneal nerve ending of Patient F1-IV5 (**H**) than a normal control (**G**). C1ORF194 protein aggregated as pale brown granules in peroneal nerve endings (**H**).

pathological features associated with CMT in Families 1 and 2 are shown in Fig. 2C–H. Electron microscopy findings of the peroneal nerves from Patient F1-IV5 (Fig. 2C–E) showed regeneration clusters and a few thinly myelinated fibres often adopting irregular shapes. Aggregated organelles were noticed in the axonal plasma. Interestingly, irregular demyelinated structures may represent defects in the axon-myelin contact and communication between the axon and Schwann cell. A biopsy of the sural nerve revealed both axonal degeneration and demyelination, consistent with the electrophysiological findings of DI-CMT in Family 1. Biopsy section of the left tibialis anterior

muscle of Patient F1-IV5 (Fig. 2F) showing muscle atrophy with hypertrophic and angulated fibres. Importantly, C1ORF194 protein aggregated as pale brown granules in peroneal nerve endings (Fig. 2G and H).

Functional analysis of mutant *C1orf194*

C1orf194 is assumed to have two alternative transcripts that encode the protein products Q5T5A4–1 and Q5T5A4–2 (Supplementary Fig. 2), respectively. The
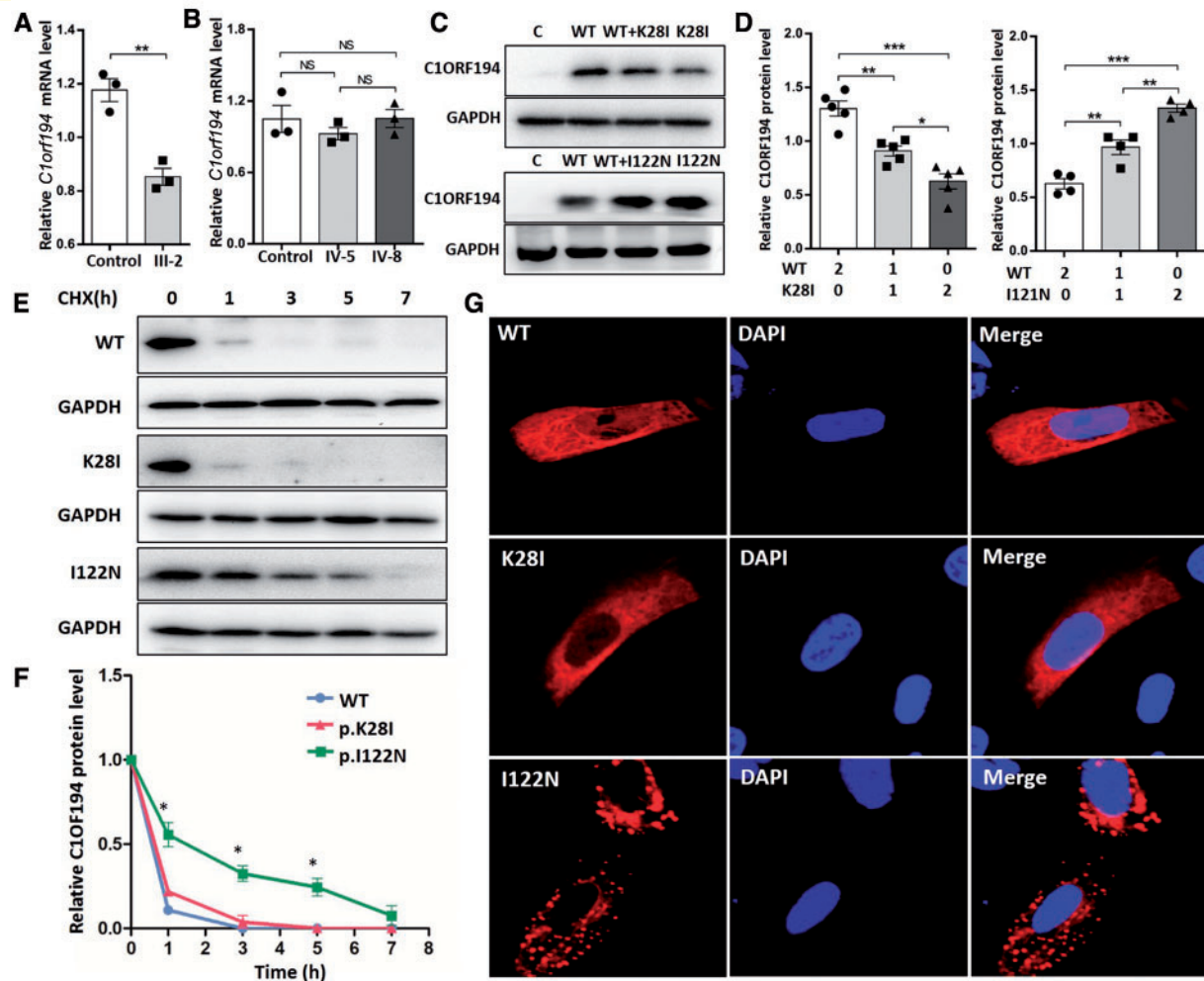
Figure 3 Effect of two mutations on C1ORF194 function. (**A** and **B**) The mRNA expression level of normal C1orf194 and two missense mutants (p.K28I and p.I122N) in white blood cells collected from normal individuals and the affected individuals (Family 1, IV-5 and IV-8; Family 2, III-2). (**C** and **D**) Overexpression of the recombinant wild-type C1ORF194 and two missense mutants (p.K28I and p.I122N) in HEK-293T cells by western blotting. (**E** and **F**) Analysis of protein stability in wild-type C1ORF194 and two missense mutants during the time course of cyclo-heximide treatment. Cell lysates containing FLAG-*C1orf194* constructs were subject to quantitative immunoblot analysis. The data of quantitative mRNA analysis or relative intensity of proteins from three independent experiments are shown in columns (**A**, **B** and **D**) and in the graph at the indicated time points (**F**). The transfection efficiency was normalized across experimental conditions. $*P < 0.05$; $**P < 0.01$; and $***P < 0.001$. (**G**) Subcellular localization of TurboFP635-tagged wild-type and two C1ORF194 mutants (p.K28I and p.I122N) in SK-N-SH neuroblastoma cells. Confocal images of C1ORF194 (red), DAPI nuclear staining (blue), and merged signals.

mRNA and protein expression analyses of the two isoforms implied that Q5T5A4–1 was the functional isoform in nerve tissues (Supplementary Fig. 2). The functional effects of two missense mutations of *C1orf194* were analysed using Q5T5A4–1 in HEK293T cells. As shown in Fig. 3A and D, the mRNA expression of the mutant c.83A>T was reduced and the p.K28I variant exerted a lower expression when the wild-type and mutant plasmids were mixed in equal proportions. However, the expression levels of the p.I122N protein were significantly increased although mutant mRNA expression was at relatively normal levels (Fig. 3B–D). This finding is in line with the extended half-life of the p.I122N protein (Fig. 3E and F). Subcellular localization studies showed that the C1ORF194 protein

was predominantly located in the cytoplasm of SK-N-SH cells, which were arranged in a microtubule cytoskeleton manner (Fig. 3G). We further demonstrated the subcellular co-localization of C1ORF194 with α-tubulin in Neuro2a cells (Supplementary Fig. 3). Although p.K28I and p.I122N did not affect localization, the p.I122N mutant protein aggregated as vesicles (Fig. 3G).

Motor and neuromuscular impairment in *C1orf194* (p.I121N) knock-in mice

Here, we showed the expression of the homologue *C1orf194* in wild-type mice from embryonic Day 15 to

adulthood (Supplementary Fig. 5A). *C1orf194* was predominantly expressed in nervous system tissues, such as the spinal cord, cerebrum, cerebellum, and sciatic nerve (Supplementary Fig. 5B and C). We generated a transgenic *C1orf194*$^{+/I121N}$ and *C1orf194*$^{I121N/I121N}$ knock-in mouse model (the homologue of the human C1ORF194 p.122N in the mouse is at position 121). Knock-in mice had a normal birth frequency that followed the classical Mendelian inheritance pattern with increased expression of *C1orf194* in mutant knock-in mice (*C1orf194*$^{+/I121N}$ and *C1orf194*$^{I121N/I121N}$, Supplementary Fig. 5D). In our model of neuropathy caused by the C1ORF194 (p.I121N) mutation, both heterozygous and homozygous knock-in mice had the phenotypes of motor and sensory neuropathy. Further observations revealed decreased body weight and motor deficits including hind limb clasping behaviour, loss of coordination, and gait abnormalities, as well as muscle weakness (Fig. 4A–J), along with reduced compound muscle action potential (CMAP) amplitudes in the peripheral nerves (Fig. K).The grip strength of knock-in mice was significantly lower than that of wild-type mice (Fig. 4I). In addition, latency to fall on an accelerating rotarod was significantly reduced in knock-in mice (Fig. 4J and Supplementary Video 1). There were no significant differences in most physiology parameters between *C1orf194*$^{+/I121N}$ and *C1orf194*$^{I121N/I121N}$ mice.

Demyelination and axonal degeneration in C1ORF194 (p.I121N) knock-in mice

Transmission electron microscopy was applied to study the ultrastructure of the sciatic nerves of the mutant mice and to observe pathological changes of myelinated nerve fibres. Electron microscopy revealed some typical CMT pathological morphological features in knock-in mice, which included extensive breakdown of compact myelin and axon degeneration (Fig. 5A–E). There was abnormal infolding of the splitting myelin sheath and contraction of the degeneration axons distributed along the fibres. Furthermore, additional myelin debris in the axonal cytoplasm were observed (Fig. 5D), which are also signs of axonal degeneration. This phenotype occurs together with a significant reduction in the G-ratio (Fig. 5F and H), smaller axon areas (Fig. 5J), and a remarkable increase in myelin thickness and abnormalities (Fig. 5G and I), reflecting degenerative alterations of the myelinated fibres. The aberrant histopathological features of *C1orf194*$^{+/I121N}$ mice (Fig. 5C) were similar to that observed in our patients with CMT disease (Fig. 2C–E). Together, these data support that knock-in of the C1ORF194 p.I121N mutation *in vivo* specifically affected both Schwann cells and axons of the sciatic nerves, which are responsible for DI-CMT neuropathies. In addition, mutant mice showed atrophy of the gastrocnemius muscle, with evidence of splitting myofibres, small clusters of angulated atrophic fibres and

fatty infiltration (Fig. 6A and C). The abundance of collagen fibres was reduced in *C1orf194*$^{+/I121N}$ mice (Fig. 6B). Moreover, immunostaining was performed to examine mouse sciatic nerves using antibodies against neurofilament 200 (Fig. 6D). As already demonstrated (Fig. 6E and F), increases in the number of Schmidt-Lanterman incisures and internodal length in mouse sciatic nerves were present, as evidence of slower transfer speeds of molecules and impaired axon-Schwann cell interactions.

The C1ORF194 protein affects signalling pathways involved in neural development and Ca^{2+} homeostasis

To identify *C1orf194*-related proteins and signalling pathways linked to CMT disease, differential expression profiling of proteins between *C1orf194*$^{+/I121N}$ and *C1orf194*$^{+/+}$ mice sciatic nerves was performed by iTRAQ coupled with LC–MS/MS analysis. SDS-PAGE verified the differential expression of proteins (Fig. 7A). A total of 3487 proteins in mouse sciatic nerve were quantitated. Using a threshold of 1.5-fold change and a coefficient of variation $\leqslant 0.05$, 329 differentially expressed proteins, including 93 downregulated proteins and 236 upregulated proteins, were found in the sciatic nerve of *C1orf194*$^{+/I121N}$ mice as compared to that of *C1orf194*$^{+/+}$ mice (data not shown). Functional categorization according to the Kyoto Encyclopedia of Genes and Genomes (KEGG) revealed that the differentially expressed proteins were mainly involved in the signaling pathway (Supplementary Fig. 6) of Parkinson's disease, Alzheimer's disease, Huntington's disease, regulation of the actin cytoskeleton, and ECM-receptor interaction, etc. We also analysed the gene ontology annotation of the differentially expressed proteins to compare the cellular components, molecular functions, and biological processes between *C1orf194*$^{+/I121N}$ and *C1orf194*$^{+/+}$ mice. The cellular components of most differentially expressed proteins were mainly enriched in the mitochondrion, myelin sheath, actin cytoskeleton, and extracellular matrix etc. (Fig. 7B). In addition, the molecular function of oxidoreductase activity, cytoskeletal protein binding, actin binding, structural constituents of the cytoskeleton, and Ca^{2+} ion binding were involved (Fig. 7C). Interestingly, upregulated expression of proteins involved in Ca^{2+} metabolism (RYR1, TNNC1, TNNC2, PVALB, ATP2A1, CASQ1, CACNA1S, VDAC1, PHKB, and MAPK12) had changed dramatically and downregulation of some of the main structural myelin proteins, including myelin basic protein (MBP) and PMP2 were also observed in *C1orf194*$^{+/I121N}$ mice (Fig. 7D). Notably, 34 proteins involved with Ca^{2+} ion binding, 12 involved with cellular Ca^{2+} ion homeostasis, and eight involved with the Ca^{2+} signalling pathways were expressed differentially (data not shown). Immunofluorescence or western blotting analysis was performed to further confirm the differential expression of COL6A2, RYR1, VDAC1, and CACNA1S (Fig.7E and F). Moreover, the mRNA expression levels of
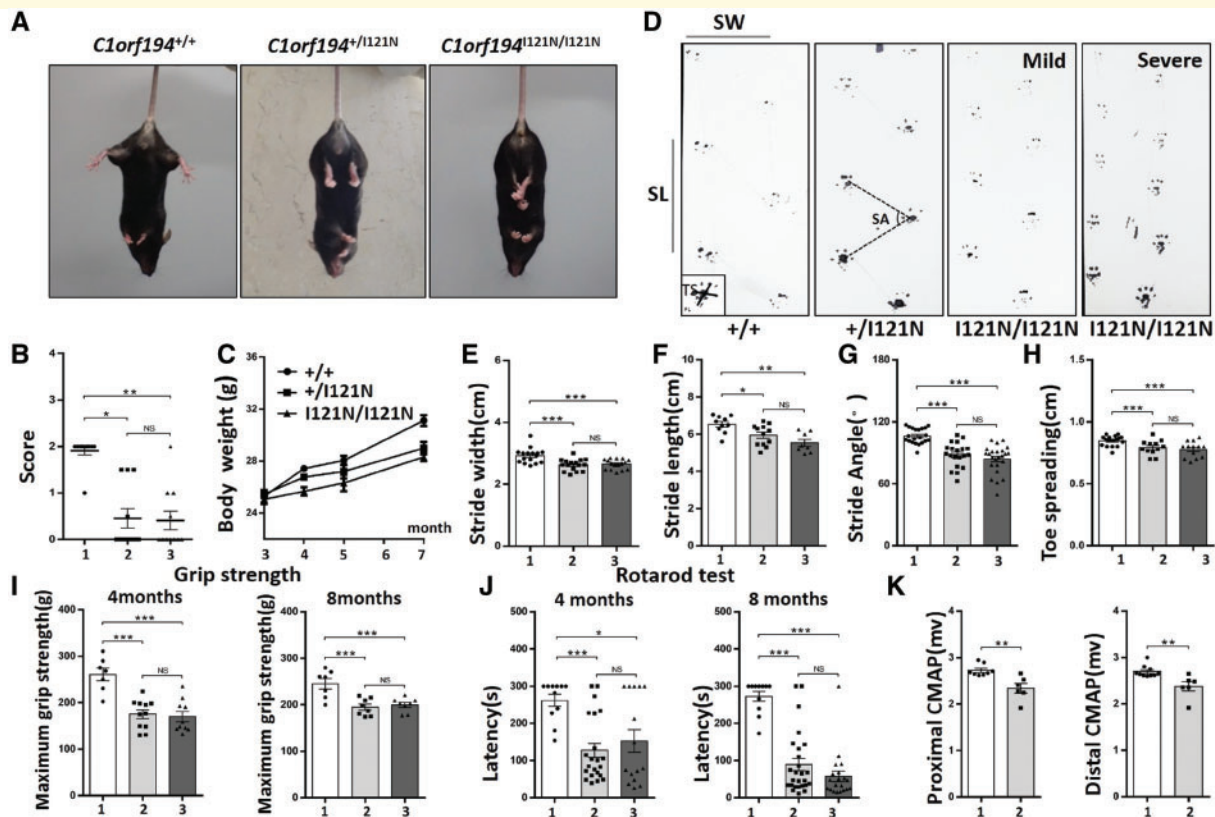
Figure 4 *C1orf194* (p.I121N) knock-in mice developed progressive motor defects and decreased muscle strength. (**A**) Hindlimb extension test of wild-type *C1orf194*$^{+/+}$ control and knock-in mice at the age of 4 months. Mice lifted by the tail showing normal spreading of the limbs (*C1orf194*$^{+/+}$), or limb-clasping behaviour (*C1orf194*$^{+/I121N}$ and *C1orf194*$^{I121N/I121N}$). (**B**) *C1orf194*$^{+/I121N}$ and *C1orf194*$^{I121N/I121N}$ mice exhibited hind limb weakness with significantly lower scores and high incidence of clasped limb. (**C**) There were significant differences in body weight between the *C1orf194*$^{+/+}$, *C1orf194*$^{+/I121N}$, and *C1orf194*$^{I121N/I121N}$ mice. (**D**) Hind limb footprints of *C1orf194*$^{+/+}$ and *C1orf194*$^{+/I121N}$, *C1orf194*$^{I121N/I121N}$ mice at the age of 4 months where the stride width (SW), stride length (SL), stride angle (SA) and toe spreading (TS) have been depicted. *C1orf194*$^{+/I121N}$ or *C1orf194*$^{I121N/I121N}$ mice exhibited disrupted walking patterns of different degrees (mild, severe). (**E–H**) Quantification of various parameters, including stride width, stride length, stride angle, and toe spreading, obtained from the gait analysis of *C1orf194*$^{+/+}$, *C1orf194*$^{+/I121N}$, and *C1orf194*$^{I121N/I121N}$ mice at the age of 4 months. (**I**) The decrease in grip strength of knock-in mice at the age of 4 and 8 months, respectively. (**J**) The obviously reduced latency of *C1orf194*$^{+/I121N}$ and *C1orf194*$^{I121N/I121N}$ mice by measurements of general motor performance using the rotarod test at the age of 4 and 8 months, respectively. (**K**) There was a marked decrease in distal and proximal CMAP in *C1orf194*$^{+/I121N}$ mice by electrophysiological testing. Data are presented as the mean ± SEM. *$P < 0.05$, **$P < 0.01$, and ***$P < 0.001$. NS = not significant. 1 = *C1orf194*$^{+/+}$ mice; 2 = *C1orf194*$^{+/I121N}$ mice; 3 = *C1orf194*$^{I121N/I121N}$ mice.

Atp2a1, *Casq1*, and *Tnnc2* was increased (Fig. 7G–I) in the sciatic nerves of *C1orf194*$^{+/+}$ mice. Therefore, we analysed the cytoplasmic Ca^{2+} ([Ca^{2+}]$_{cyto}$) and mitochondrial Ca^{2+} ([Ca^{2+}]$_{mito}$) concentrations in transfected SHSY5Y cells by recombinant lentivirus-mediated p.I122N variant or wild-type C1ORF194. The results showed that [Ca^{2+}]$_{cyto}$ was significantly increased in SHSY5Y cells transfected with p.I122N variant, as compared to wild-type C1ORF194 (Fig. 7J), whereas [Ca^{2+}]$_{mito}$ was significantly lower in mutant cells than wild-type control cells (Fig. 7K). Simultaneously, the significant reduction of ATP (Fig. 7L) was observed in mutant cells than wild-type control cells. Furthermore, we also detected the increased [Ca^{2+}]$_{cyto}$ concentration in IMR-32 cells transfected with recombinant K28I (Fig. 7M).

Discussion

In this study, we identified two heterozygous missense mutations in *C1orf194*, p.I122N and p.K28I, which were genetically linked to CMT disease in two unrelated families. Functional study implied that mutant C1ORF194 protein disrupted signalling pathways involved in Ca^{2+} homeostasis and caused CMT. However, the results of the present study showed that inter-familial genetic heterogeneity was associated with different types of CMT in the two families studied (Table 1). Specifically, the p.I122N missense mutation led to an intermediate form of CMT in Family 1, while the p.K28I missense mutation was predominantly the cause of the demyelinating form of CMT in Family 2. In fact, high clinical and genetic heterogeneity was present in CMT
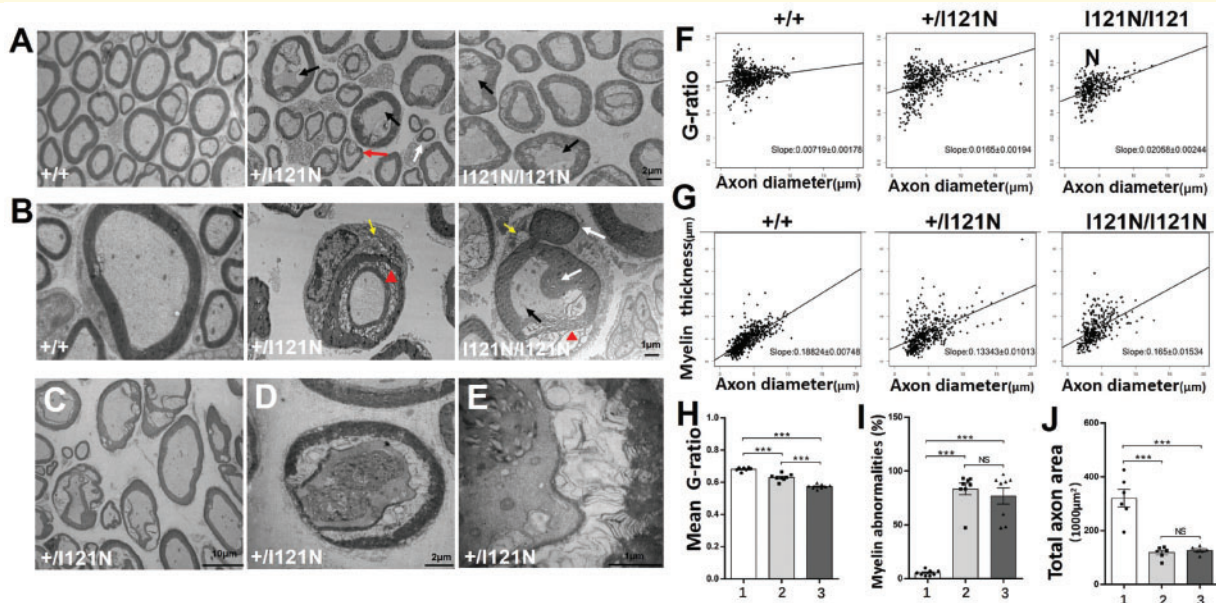
Figure 5 Demyelination and axonal degeneration in *C1orf194* (p.I121N) knock-in mice. (**A** and **B**) Transmission electron micrographs of the sciatic nerves of *C1orf194*$^{+/I121N}$ and *C1orf194*$^{I121N/I121N}$ knock-in mice, as compared with those of wild-type *C1orf194*$^{+/+}$ controls at the age of 4 months. The mutant mice clearly showed irregular small fibres (red arrows), external and internal myelin folding (white arrows), myelin breakdown (red arrowheads), lipid droplets in Schwann cells (yellow arrows) and compression of the axon (black arrows). (**C**) Irregular demyelinated structure in the sciatic nerves of *C1orf194*$^{+/I121N}$ mice recapitulate the pathology features of the peroneal nerves from Patient F1-IV5. (**D**) Axonal degeneration in the sciatic nerves of *C1orf194*$^{+/I121N}$ mice. (**E**) Higher magnification images from (**D**). Scatter plots of G-ratios (**F**), as calculated by dividing the axon diameter by the fibre diameter. (**G**) Scatter plots of myelin thicknesses. Each point corresponds to one fibre. (**H**) Average G-ratios were higher in wild-type mice (0.679332 ± 0.006407) than mutant mice (0.648464 ± 0.010403 in heterozygotes and 0.592559 ± 0.009071 in homozygotes). (**I**) The percentage of myelin profiles for three genotypes of knock-in mice, showing increased myelin abnormalities in mutant mice. (**J**) Quantification of the axon area of sciatic nerves for three genotypes of mice, showing significant decreases in knock-in mice. Data are presented as the mean ± SEM from **H** and **J**. ***$P < 0.001$. NS = not significant; 1 = *C1orf194*$^{+/+}$ mice; 2 = *C1orf194*$^{+/I121N}$ mice; 3 = *C1orf194*$^{I121N/I121N}$ mice.

disease. The phenotypic heterogeneity of CMT may also be caused by different mutations in the same gene, such as *MPZ*, *NEFL*, *GDAP1*, and *DNM2* (Claramunt *et al.*, 2005; Zuchner *et al.*, 2005; Fabrizi *et al.*, 2007; Maeda *et al.*, 2012; Bombelli *et al.*, 2014; Karakaya *et al.*, 2017). Moreover, the p.K28I variant significantly reduced expression of the C1ORF194 protein, while the p.I122N variant increased levels (Fig. 3C and D). In addition, the p.I122N mutant protein had aggregated in vesicles of transfected SK-N-SH cells, which increased its stability, but this phenomenon was not present with the p.K28I mutant protein. We hypothesize that either partial loss- or gain-of-function mechanisms of CMT linked to *C1orf194* mutations may partly explain the phenotypic heterogeneity of this disease in our patients, as reported previously in CMT2D/CMT1E patients with loss- or gain-of-function mutations to *PMP22* (Sakakura *et al.*, 2011; Li *et al.*, 2013). Moreover, the distinct *MPZ* mutations have been reported to result in distinct peripheral neuropathy (Shy *et al.*, 2004). These mutations disrupt the MPZ structure, which predominantly affects myelination during development and causes early onset of disease, and those predominantly affect Schwann cell-axonal interactions cause late

onset disease. Mutations in the last exon of *MPZ* (Shy *et al.*, 2004) also resulted in a greater protein accumulation (Matsuyama *et al.*, 2002; Shy *et al.*, 2004), which is the same as the p.I122N mutant in *C1orf194* (Figs 2H and 3D), potentially leading to gain-of-function of stably mutant proteins.

To examine the effects of the p.I122N substitution on peripheral nerve development further, we generated a knock-in mouse model. The *C1orf194* p.I121N knock-in mice develop peripheral neuropathy, which show several key features of motor and neuromuscular defects that mimic the phenotype of DI-CMT. The sciatic nerves of the knock-in mice (Fig. 5) with degenerated axons and collapsed myelin are well matched with the pathological findings of the sural nerve biopsies of the patient (Fig. 2) in this study. We observed myelin splitting and degeneration in association with extensively constricted axons. Both axonal defects and demyelinating neuropathies imply that C1ORF194 is vital for the development of myelinated fibres. In addition, we also generated a *C1orf194* knock-out mouse model that also presented the CMT phenotypes (data not shown). These findings strongly suggest that *C1orf194* is important for the maintenance of myelin-
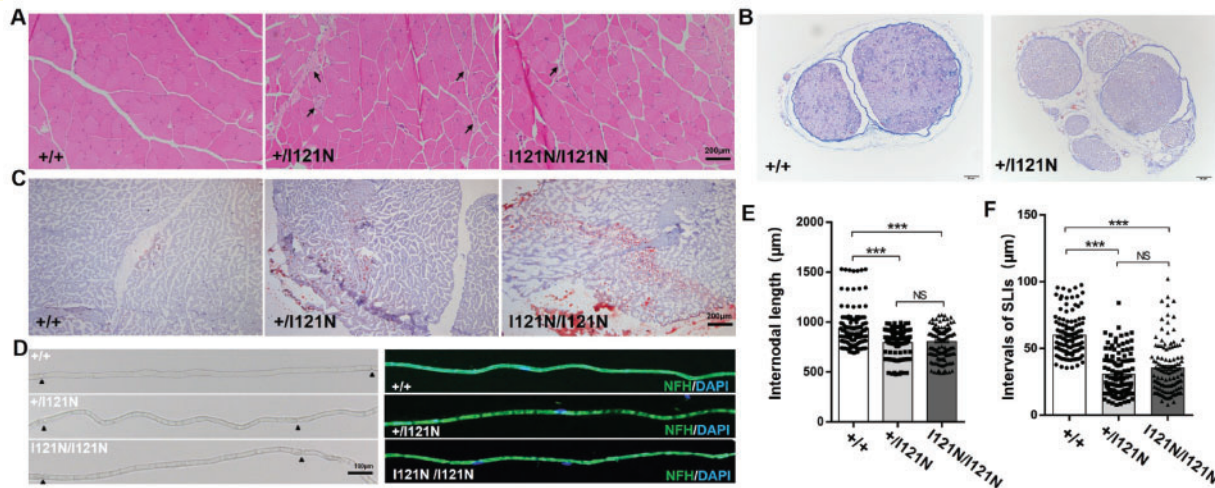
Figure 6 Neuromuscular morphological alteration in *C1orf194* (p.I121N) knock-in mice. (**A**) Haematoxylin and eosin staining of the gastrocnemius muscles of *C1orf194*$^{+/+}$, *C1orf194*$^{+/I121N}$, and *C1orf194*$^{I121N/I121N}$ mice. Note that the normal muscle of *C1orf194*$^{+/+}$ mice contained polygonal-shaped myofibres that were uniform in shape and size, while there was angulated atrophic myofibres (black arrowheads) and necrosis in the muscle tissue of *C1orf194*$^{+/I121N}$ and *C1orf194*$^{I121N/I121N}$ mice. (**B**) Normal sciatic nerve collagen fibres (blue) surrounded the perineurium, or were located among the myelin sheaths, while the abundance of collagen fibres was reduced in *C1orf194*$^{+/I121N}$ mice. (**C**) Evaluation of the fatty infiltration of the gastrocnemius muscles of *C1orf194*$^{+/+}$, *C1orf194*$^{+/I121N}$, and *C1orf194*$^{I121N/I121N}$ mice by Oil red O staining showed a significant increase in the percentage of fat in the *C1orf194*$^{+/I121N}$ and *C1orf194*$^{I121N/I121N}$ mice. (**D**) Shortened internodal segments (arrow) were observed in sciatic nerves of *C1orf194*$^{+/I121N}$ and *C1orf194*$^{I121N/I121N}$ mice. Immunostaining of mouse sciatic nerves using NFH200 antibody revealed abnormal distribution of neurofilaments and a greater occurrence of SLIs in *C1orf194*$^{+/I121N}$ and *C1orf194*$^{I121N/I121N}$ knock-in mice. (**E**) Intervals of Schmidt-Lanterman incisures were compared among the *C1orf194*$^{+/+}$, *C1orf194*$^{+/I121N}$, and *C1orf194*$^{I121N/I121N}$ mice. (*n* = 129, 132, and 154, respectively). (**F**) A comparison among all three mouse models showed that the mean internodal length in *C1orf194*$^{+/I121N}$ (*n* = 125) and *C1orf194*$^{I121N/I121N}$ (*n* = 118) mice was significantly shorter than that in *C1orf194*$^{+/+}$ mice (*n* = 113) (792.53 ± 22.0 and 803.88 ± 24.5 versus 948.49 ± 38.4 μm, respectively). Data are presented as the mean ± SEM from **B**. ***$P < 0.001$. NS = not significant.

axon integrity. We suggest a putative role for *C1orf194* in the interaction between Schwann cells and axons that, when interrupted, may cause either axonal degeneration or demyelination in the peripheral nerves.

Furthermore, mutations in the C1ORF194 protein affect a number of proteins and signalling pathways in nervous system, as determined by the proteomics study, suggesting a role in myelination of the peripheral nervous system. Notably, we focused on the proteins with the greatest amount of change. Dysregulation of Ca^{2+} homeostasis has been attributed to the molecular pathogenesis of numerous neurodegenerative and muscle disorders (Fernyhough and Calcutt, 2010; Wang *et al.*, 2013; Logan *et al.*, 2014; Gonzalez-Sanchez *et al.*, 2017). Wallerian degeneration is mediated by extracellular Ca^{2+} influx, which is characterized by the loss of axon structure and fragmentation of myelin structures. An increase in intracellular Ca^{2+} induced the dedifferentiation of Schwann cells. C1ORF194 upregulated protein expression of the Ca^{2+} channel-associated proteins RYR1, TNNC1, TNNC2, PVALB, ATP2A1, CASQ1, and CACNA1S. These are the key calcium cycling proteins that correlated to sarcoplasmic reticulum release and uptake of Ca^{2+} (Kraner *et al.*, 2011; Manttari *et al.*, 2013; Canato *et al.*, 2015). Therefore, we examined cytoplasmic Ca^{2+} responses and found alterations in transfected cells expressing

the mutant C1ORF194. The results of this study validated the enhancement of $[Ca^{2+}]_{cyto}$ in stable SYSH5Y cell lines transfected with C1ORF194 harbouring the p.I122N mutation. These data suggest that C1ORF194 plays a relevant role in Ca^{2+} release. We propose C1ORF194, a novel Ca^{2+} regulator, as a potential target in other neurodegenerative disorders characterized by altered Ca^{2+} homeostasis. To evaluate the role of C1ORF194 in chaperone-associated Ca^{2+} homeostasis further, we subsequently investigated the effects of p.K28I mutations on intracellular alterations of Ca^{2+} dynamics in mutant transfected SYSH5Y cells. Interestingly, increased intracellular Ca^{2+} concentrations were also observed. Therefore, we deduced the mutant C1ORF194 led to abnormalities of Ca^{2+} homeostasis to cause cell demyelination and axonal degeneration. C1ORF194 is an uncharacterized protein of unknown function (DUF3695), thus its functions and the mechanisms resulting in peripheral neuropathies remain to be elucidated. Therefore, we were unable to conclude whether the genetic mechanisms of these two mutations are associated with a gain- or loss-of-function. However, it seems that either gain- or loss-of-function might linked to dysregulation of Ca^{2+} homeostasis, indicating that these two different mutations may share a common pathway in myelination of the peripheral nervous system.
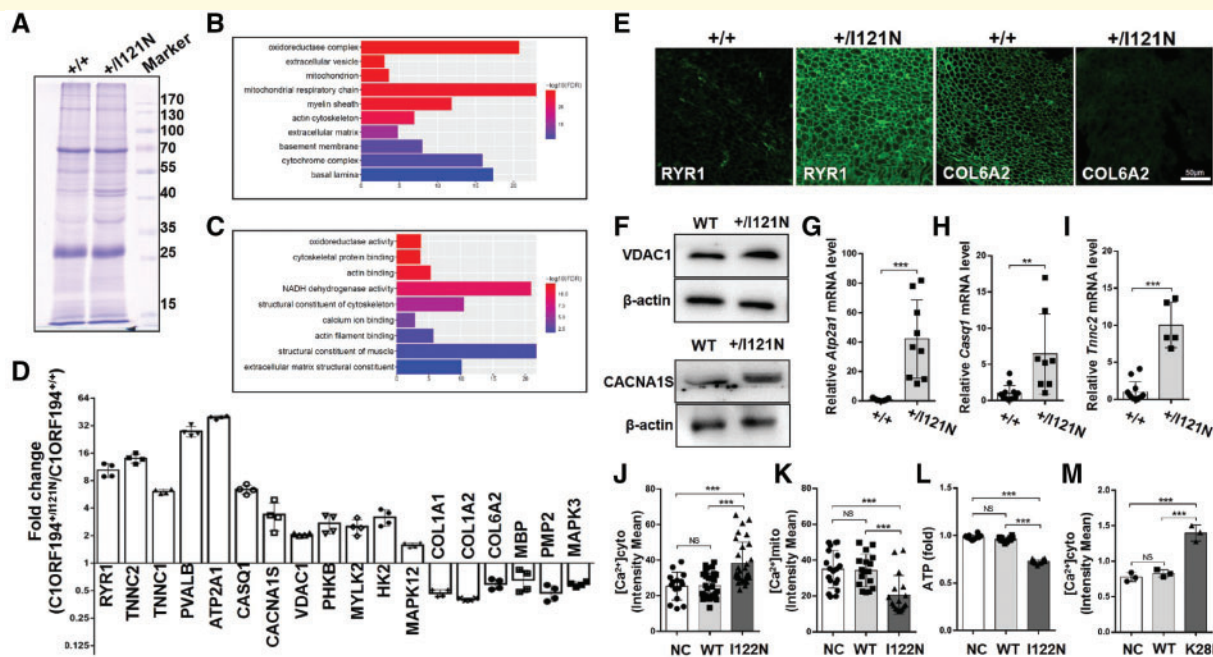
Figure 7 Mutant C1ORF194 proteins affect the expression profiles of calcium ion binding proteins. (**A**) SDS-PAGE electrophoresis of differentially expressed proteins in the mouse sciatic nerves between *C1orf194*$^{+/I121N}$ and *C1orf194*$^{+/+}$ mice. (**B** and **C**) GO annotation of 329 differentially expressed proteins from the sciatic nerve between *C1orf194*$^{+/I121N}$ and *C1orf194*$^{+/+}$ mice identified and quantified by iTRAQ coupled with LC-MS/MS analysis. (**B**) The cellular components of most differentially expressed proteins were mainly enriched in the mitochondria, actin cytoskeleton, extracellular matrix and myelin sheaths, etc. (**C**) The molecular function of most differentially expressed proteins was related to oxidoreductase activity, cytoskeletal protein binding, and calcium ion binding, etc. (**D**) iTRAQ coupled with LC–MS/MS analysis of differentially expressed proteins from the sciatic nerves between *C1orf194*$^{+/I121N}$ and *C1orf194*$^{+/+}$ mice. Upregulated expression of proteins involved in Ca^{2+} metabolism (RYR1, TNNC1, TNNC2, PVALB, ATP2A1, CASQ1, CACNA1S, VDAC1, PHKB, MYLK2, HK2 and MAPK12) and down-regulation of some of the main structural myelin proteins, including MBP and PMP2 in *C1orf194*$^{+/+}$ mice. Moreover, proteins levels of COL1A1, COL1A2, COL6A2 and MAPK3 were downregulated in *C1orf194*$^{+/+}$ mice. (**E**) By immunofluorescence analysis, the protein levels of RYR1 in the sciatic nerves of *C1orf194*$^{+/I121N}$ mice were significantly increased. Expression levels of COL6A2 were significantly decreased. (**F**) By immunoblot analysis, the protein levels of VDAC1 and CACNA1S in the spinal cords of *C1orf194*$^{+/I121N}$ and *C1orf194*$^{+/+}$ mice were normalized to β-actin. (**G–I**) By real-time quantitative PCR analysis, the mRNA expression levels of *Atp2a1*, *Casq1*, and *Tnnc2* was significantly increased and *Mbp* was significantly decreased in the sciatic nerves of *C1orf194*$^{+/I121N}$ mice. (**J** and **K**) Quantitative measurements of intracellular and mitochondrial Ca^{2+} alterations in stably I122N-transfected or wild-type control SH-SY5Y cells, as determined by confocal microscopy. (**L**) The amount of ATP was decreased in stably I122N-transfected SH-SY5Y cells. (**M**) Quantitative measurements of [Ca^{2+}]$_{cyto}$ in IMR-32 cells transfected with recombinant K28I plasmid, as determined by flow cytometry with preload flu-3AM. The relative intensity of the data generated from three replicates are shown in the columns with standard errors indicated by bars. **P < 0.01; ***P < 0.001; NS = not significant.

In conclusion, we discovered a new pathogenic gene, *C1orf194*, which causes CMT disease. A transgenic mouse model was used to recapitulate the hallmark features of the disease. The novel protein encoded by the *C1orf194* gene was found to play a critical role in the development of the peripheral nerves, which was associated with the regulation of Ca^{2+} homeostasis linked to CMT. Our study extends the phenotypical variability in CMT linked to *C1orf194* mutations and provides clues to its pathogenesis. Further investigations are needed to elucidate the biological functions of *C1orf194* contributing to cellular Ca^{2+} homeostasis.

Web resources

GenBank, http://www.ncbi.nlm.nih.gov/Genbank/
Online Medelian Inheritance in Man (OMIM), http://www.omim.org/

UCSC Genome Browser, http://www.genome.ucsc.edu/
NCBI BLAST, http://www.ncbi.nlm.nih.gov/blast/
ExAC, http://exac.broadinstitute.org/
YH Genomes, http://yh.genomics.org.cn/
1000 Genomes, http://www.1000genomes.org/
Mouse Genome Informatics, http://www.informatics.jax.org/
RefSeq, https://www.ncbi.nlm.nih.gov/refseq/

Acknowledgements

Funding

Competing interests

The authors declare no competing financial interests.

Supplementary material

Supplementary material is available at *Brain* online.

References

Barreto LC, Oliveira FS, Nunes PS, de Franca Costa IM, Garcez CA, Goes GM, et al. Epidemiologic study of Charcot-Marie-Tooth disease: a systematic review. Neuroepidemiology 2016; 46: 157–65.

Berciano J, Garcia A, Gallardo E, Peeters K, Pelayo-Negro AL, Alvarez-Paradelo S, et al. Intermediate Charcot-Marie-Tooth disease: an electrophysiological reappraisal and systematic review. J Neurol 2017; 264: 1655–77.

Bombelli F, Stojkovic T, Dubourg O, Echaniz-Laguna A, Tardieu S, Larcher K, et al. Charcot-Marie-Tooth disease type 2A: from typical to rare phenotypic and genotypic features. JAMA Neurol 2014; 71: 1036–42.

Canato M, Capitanio P, Reggiani C, Cancellara L. The disorders of the calcium release unit of skeletal muscles: what have we learned from mouse models? J Muscle Res Cell Motil 2015; 36: 61–9.

Claramunt R, Pedrola L, Sevilla T, Lopez de Munain A, Berciano J, Cuesta A, et al. Genetics of Charcot-Marie-Tooth disease type 4A: mutations, inheritance, phenotypic variability, and founder effect. J Med Genet 2005; 42: 358–65.

Delphine B, Manisha J, Istvan K, Anne H, Bob A, Vicky D W, et al. A knock-in/knock-out mouse model of HSPB8-associated distal hereditary motor neuropathy and myopathy reveals toxic gain-of-function of mutant Hspb8. Acta Neuropathol 2018; 135: 131–48.

Donate-Macian P, Jungfleisch J, Perez-Vilaro G, Rubio-Moscardo F, Peralvarez-Marin A, Diez J, et al. The TRPV4 channel links calcium influx to DDX3X activity and viral infectivity. Nat Commun 2018; 9: 2307.

Fabrizi GM, Cavallaro T, Angiari C, Cabrini I, Taioli F, Malerba G, et al. Charcot-Marie-Tooth disease type 2E, a disorder of the cytoskeleton. Brain 2007; 130 (Pt 2): 394–403.

Fernyhough P, Calcutt NA. Abnormal calcium homeostasis in peripheral neuropathies. Cell Calcium 2010; 47: 130–9.

Gonzalez-Sanchez P, Pla-Martin D, Martinez-Valero P, Rueda CB, Calpena E, Del Arco A, et al. CMT-linked loss-of-function mutations in GDAP1 impair store-operated Ca(2 +) entry-stimulated respiration. Sci Rep 2017; 7: 42993.

Harel T, Lupski JR. Charcot-Marie-Tooth disease and pathways to molecular based therapies. Clin Genet 2014; 86: 422–31.

Hoyle JC, Isfort MC, Roggenbuck J, Arnold WD. The genetics of Charcot-Marie-Tooth disease: current trends and future implications for diagnosis and management. Appl Clin Genet 2015; 8: 235–43.

Karakaya M, Mazaheri N, Polat I, Bharucha-Goebel D, Donkervoort S, Maroofian R, et al. Biallelic MCM3AP mutations cause Charcot-Marie-Tooth neuropathy with variable clinical presentation. Brain 2017; 140: e65.

Kraner SD, Wang Q, Novak KR, Cheng D, Cool DR, Peng J, et al. Upregulation of the CaV 1.1-ryanodine receptor complex in a rat model of critical illness myopathy. Am J Physiol Regul Integr Comp Physiol 2011; 300: R1384–91.

Lassuthova P, Rebelo AP, Ravenscroft G, Lamont PJ, Davis MR, Manganelli F, et al. Mutations in ATP1A1 cause dominant Charcot-Marie-Tooth type 2. Am J Hum Genet 2018; 102: 505–14.

Li J, Parker B, Martyn C, Natarajan C, Guo J. The PMP22 gene and its related diseases. Mol Neurobiol 2013; 47: 673–98.

Logan CV, Szabadkai G, Sharpe JA, Parry DA, Torelli S, Childs AM, et al. Loss-of-function mutations in MICU1 cause a brain and muscle disorder linked to primary alterations in mitochondrial calcium signaling. Nat Genet 2014; 46: 188–93.

Maeda MH, Mitsui J, Soong BW, Takahashi Y, Ishiura H, Hayashi S, et al. Increased gene dosage of myelin protein zero causes Charcot-Marie-Tooth disease. Ann Neurol 2012; 71: 84–92.

Manttari S, Ortenblad N, Madsen K, Pilegaard H. Both short intense and prolonged moderate in vitro stimulation reduce the mRNA expression of calcium-regulatory proteins in rat skeletal muscle. Mol Cell Biochem 2013; 373: 171–8.

Matsuyama W, Nakagawa M, Takashima H, Osame M. Altered trafficking and adhesion function of MPZ mutations and phenotypes of Charcot-Marie-Tooth disease 1B. Acta Neuropathol 2002; 103: 501–8.

Pareyson D, Saveri P, Pisciotta C. New developments in Charcot-Marie-Tooth neuropathy and related diseases. Curr Opin Neurol 2017; 30: 471–80.

Prior R, Van Helleputte L, Benoy V, Van Den Bosch L. Defective axonal transport: a common pathological mechanism in inherited and acquired peripheral neuropathies. Neurobiol Dis 2017; 105: 300–20.

Rossor AM, Polke JM, Houlden H, Reilly MM. Clinical implications of genetic advances in Charcot-Marie-Tooth disease. Nat Rev Neurol 2013; 9: 562–71.

Sakakura M, Hadziselimovic A, Wang Z, Schey KL, Sanders CR. Structural basis for the Trembler-J phenotype of Charcot-Marie-Tooth disease. Structure 2011; 19: 1160–9.

Shy ME, Jani A, Krajewski K, Grandis M, Lewis RA, Li J, et al. Phenotypic clustering in MPZ mutations. Brain 2004; 127 (Pt 2): 371–84.

Sociali G, Visigalli D, Prukop T, Cervellini I, Mannino E, Venturi C, et al. Tolerability and efficacy study of P2X7 inhibition in experimental Charcot-Marie-Tooth type 1A (CMT1A) neuropathy. Neurobiol Dis 2016; 95: 145–57.

Villegas R, Martinez NW, Lillo J, Pihan P, Hernandez D, Twiss JL, et al. Calcium release from intra-axonal endoplasmic reticulum leads to axon degeneration through mitochondrial dysfunction. J Neurosci 2014; 34: 7179–89.

Wang JQ, Chen Q, Wang X, Wang QC, Wang Y, Cheng HP, et al. Dysregulation of mitochondrial calcium signaling and superoxide flashes cause mitochondrial genomic DNA damage in Huntington disease. J Biol Chem 2013; 288: 3070–84.

Yang Q, Chen D, Xiong F, Chen D, Liu C, Liu Y, et al. A splicing mutation in VPS4B causes dentin dysplasia I. J Med Genet 2016; 53: 624–33.

Zhang Z, David G. Stimulation-induced Ca(2 +) influx at nodes of Ranvier in mouse peripheral motor axons. J Physiol 2016; 594: 39–57.

Zhao X, Li X, Hu Z, Liu L, Xie Y, Tian T, et al. MORC2 mutations in a cohort of Chinese patients with Charcot-Marie-Tooth disease type 2. Brain 2016; 139 (Pt 10): e56.

Zuchner S, Noureddine M, Kennerson M, Verhoeven K, Claeys K, De Jonghe P, et al. Mutations in the pleckstrin homology domain of dynamin 2 cause dominant intermediate Charcot-Marie-Tooth disease. Nat Genet 2005; 37: 289–94.